J Solid State Electrochem (2008) 12:15–30
DOI 10.1007/s10008-007-0353-x

ORIGINAL PAPER

Behavior of $(La,Sr)CoO_3$- and La_2NiO_4-based ceramic anodes in alkaline media: compositional and microstructural factors

S. K. Poznyak · V. V. Kharton · J. R. Frade · A. A. Yaremchenko · E. V. Tsipis · S. O. Yakovlev · I. P. Marozau

Received: 15 March 2007 / Revised: 23 April 2007 / Accepted: 3 May 2007 / Published online: 13 June 2007

Abstract The behavior of dense ceramic anodes made of perovskite-type $La_{1-x-y}Sr_xCo_{1-z}Al_zO_{3-\delta}$ (x=0.30–0.70; y=0–0.05; z=0–0.20) and K_2NiF_4-type $La_2Ni_{1-x}Me_xO_{4+\delta}$ (Me=Co, Cu; x=0–0.20) indicates significant influence of metal hydroxide formation at the electrode surface on the oxygen evolution reaction (OER) kinetics in alkaline solutions. The overpotential of cobaltite electrodes was found to decrease with time, while cyclic voltammetry shows the appearance of redox peaks characteristic of $Co(OH)_2$/CoOOH. This is accompanied with increasing effective capacitance estimated from the impedance spectroscopy data, because of roughening of the ceramic surface. The steady-state polarization curves of $(La,Sr)CoO_{3-\delta}$ in the OER range, including the Tafel slope, are very similar to those of model $Co(OH)_2$–$La(OH)_3$ composite films where the introduction of lanthanum hydroxide leads to decreasing electrochemical activity. La_2NiO_4-based anodes exhibit a low electrochemical performance and poor stability. The effects of oxygen nonstoichiometry of the perovskite-related phases are rather negligible at high overpotentials but become significant when the polarization decreases, a result of increasing role of oxygen intercalation processes. The maximum electrocatalytic activity to OER was observed for A-site-deficient $(La_{0.3}Sr_{0.7})_{0.97}CoO_{3-\delta}$, where the lanthanum content is relatively low and the Co^{4+} concentration determined by thermogravimetric analysis is highest compared to other cobaltites. Applying microporous layers made of template-synthesized nanocrystalline $(La_{0.3}Sr_{0.7})_{0.97}CoO_{3-\delta}$ leads to an improved anode performance, although the effects of microstructure and thickness are modest, suggesting a narrow electrochemical reaction zone. Further enhancement of the OER kinetics can be achieved by electrodeposition of cobalt hydroxide- and nickel hydroxide-based films.

Keywords Oxygen evolution · Perovskite-related oxide · Lanthanum–strontium cobaltite · Lanthanum nickelate · Electrocatalytic activity · Degradation · Oxygen intercalation

Introduction

Electrochemical evolution and reduction of oxygen in alkaline media are of considerable interest for numerous technological applications, including secondary metal–air batteries, water electrolysis, low-temperature fuel cells, electrosynthesis, and metal processing. Very high electrocatalytic activity for the oxygen evolution reaction (OER) in alkaline solutions is known for numerous transition metal oxide-based materials, in particular for Ni- and Co-containing perovskite-related compounds [1–7]. However, despite the extensive investigations in this field, literature data on the relationships between the electrochemical behavior and composition of perovskite-related phases, such as $La_{1-x}Sr_xCoO_{3-\delta}$, are often contradictory. For instance, early works [5, 6, 8–12] were centered on the behavior of ceramic $La_{1-x}Sr_xCoO_{3-\delta}$ electrodes prepared by the standard solid-state reaction route, which is associated with significant variations in the porosity and,

Dedicated to Professor Dr. Yakov I. Tur'yan on the occasion of his 85th birthday.

S. K. Poznyak · V. V. Kharton (✉) · J. R. Frade · A. A. Yaremchenko · E. V. Tsipis · S. O. Yakovlev · I. P. Marozau
Department of Ceramics and Glass Engineering, CICECO, University of Aveiro,
3810-193 Aveiro, Portugal
e-mail: kharton@cv.ua.pt

thus, specific surface area. Bockris and Otagawa [5] and Matsumoto et al. [6] observed that the electrocatalytic activity of $La_{1-x}Sr_xCoO_{3-\delta}$ (x=0–0.4) increases with x. Later, highly dispersed $(La,Sr)CoO_{3-\delta}$ film electrodes fabricated using a low temperature sol–gel process and carbonate precipitation method were studied in a wider compositional range [13–16]; the true electrochemical activity assessed taking the real surface area into account was found to decrease when strontium content increases [16]. A similar discrepancy in the literature data relates to the OER order with respect to the hydroxide concentration. This value was reported as 1.8 for $La_{1-x}Sr_xCoO_{3-\delta}$ (x=0.2, 0.4) [6] and 0.6–0.8 for $La_{0.5}Sr_{0.5}CoO_{3-\delta}$ [11], whereas other authors [5, 8, 13–16] observed the reaction order close to unity. Such discrepancies may result from the use of different synthesis methods and processing conditions. Information on the role of microstructural factors, particularly possible compositional changes in the ceramic anodes near the interface [9, 10], is still scarce. Therefore, although a large surface area is desirable for practical applications, optimization of the electrode compositions requires to reassess electrochemical properties of high-density ceramic materials, all synthesized by the same method and studied under similar conditions. The compositions with maximum performance can then be used to develop highly porous electrode structures.

The present work was focused on the comparative analysis of electrochemical behavior of dense anodes including perovskite-type $La_{1-x-y}Sr_xCo_{1-z}Al_zO_{3-\delta}$ (x= 0.30–0.70; y=0–0.05; z=0–0.20) and $La_2Ni_{1-x}Me_xO_{4+\delta}$ (Me=Co, Cu; x=0–0.20) with K_2NiF_4 structure, and multilayered electrodes comprising microporous template-synthesized $(La,Sr)CoO_{3-\delta}$ deposited onto dense cobaltite ceramics, in alkaline media. The K_2NiF_4-type nickelates were selected for the study, as $La_2NiO_{4+\delta}$ is the only thermodynamically stable compound in the La–Ni–O system at atmospheric oxygen pressure and elevated temperatures necessary to sinter high-density ceramics [17, 18], although the conductivity and nickel oxidation state in these phases are lower compared to $LaNiO_3$-based compounds. To provide similar morphology of dense ceramic anodes, the corresponding materials were all synthesized by the glycine-nitrate process (GNP), a self-combustion technique using glycine as a fuel and chelating agent and nitrates of metal components as the oxidant [19]. This method is well known as suitable to obtain fine and homogeneous multicomponent oxide powders [19]. The same technique and the cellulose-precursor method [20] were employed for the synthesis of nanocrystalline powders, used for the fabrication of porous layers.

Experimental

In the course of GNP, glycine was added into aqueous solutions containing metal nitrates in the stoichiometric proportion. The glycine/nitrate molar ratio was 1.5–2.0 of stoichiometric, calculated assuming that the only gaseous products of reaction are N_2, CO_2, and H_2O. After drying and combustion, the resultant powders were annealed at 900–1,100 °C for 2 h to remove organic residuals, ball-milled, and then pressed (120–250 MPa). Ceramics with a density higher than 93% of their theoretical density calculated from X-ray diffraction (XRD) data were sintered in air at 1,250–1,430 °C for 5 h. The samples were finally annealed in air at 1,000 °C for 3–4 h and slowly cooled to retain equilibrium with atmospheric oxygen at low temperatures. For the preparation of porous layers, the cation-deficient $(La_{0.3}Sr_{0.7})_{0.97}CoO_{3-\delta}$ perovskite exhibiting a relatively high conductivity (Table 1) in combination with a good electrocatalytic activity for the OER was selected. The nanocrystalline powders of $(La_{0.3}Sr_{0.7})_{0.97}CoO_{3-\delta}$ were synthesized using three different cellulose precursors namely, jeans type, cotton-textile type, and cotton bandage

Table 1 Properties of the ceramic electrode materials at room temperature

Composition	Phase impurities	Structure	Unit cell parameters (nm)	δ	Conductivity (S cm^{-1})
$La_{0.3}Sr_{0.7}CoO_{3-\delta}$	–	Perovskite	a=0.3836	0.076	2.1×10^3
$La_{0.3}Sr_{0.7}Co_{0.8}Al_{0.2}O_{3-\delta}$	–	Perovskite	a=0.3846	0.150	5.4×10^2
$(La_{0.3}Sr_{0.7})_{0.97}CoO_{3-\delta}$	–	Perovskite	a=0.3837	0.104	3.6×10^3
$La_{0.5}Sr_{0.5}CoO_{3-\delta}$	–	Perovskite	a=0.5424, α=59.93^0	<0.003	4.0×10^3
$La_{0.55}Sr_{0.40}CoO_{3-\delta}$	CoO	Perovskite	a=0.5418, α=60.14^0	–	3.8×10^3
$La_{0.65}Sr_{0.30}CoO_{3-\delta}$	CoO	Perovskite	a=0.5409, α=60.27^0	<0.003	5.0×10^3
$La_{0.7}Sr_{0.3}CoO_{3-\delta}$	–	Perovskite	a=0.5404, α=60.43^0	<0.003	4.2×10^3
$La_2NiO_{4+\delta}$	–	K_2NiF_4-type	a=0.3865, c=1.2691	0.150	39
$La_2Ni_{0.9}Co_{0.1}O_{4+\delta}$	–	K_2NiF_4-type	a=0.3864, c=1.2664	0.169	3.8
$La_2Ni_{0.8}Cu_{0.2}O_{4+\delta}$	–	K_2NiF_4-type	a=0.3858, c=1.2787	0.124	24

type (designated as A, B, and C); the technique is described elsewhere [20]. All materials were annealed at 900 °C for 2 h and dispersed in ethanol. The porous layers, hereafter referred to as A/$La_{1-x}Sr_xCoO_{3-\delta}$, B/$La_{1-x}Sr_xCoO_{3-\delta}$, or C/$La_{1-x}Sr_xCoO_{3-\delta}$, were applied onto polished dense ceramic substrates and then sintered at 1,200 °C for 2 h. The same procedure was used to prepare porous layers of the GNP-synthesized powder (referred to as GNP/$La_{1-x}Sr_xCoO_{3-\delta}$) and the anodes with two porous layers. The electrodes of latter series, tested to assess the effects of near-surface microstructure, comprise one layer made of a nanocrystalline powder (synthesized from the cellulose precursor, type A) and a top layer of grained cobaltite denoted as G-$(La_{0.7}Sr_{0.3})_{0.97}CoO_{3-\delta}$.

Characterization of the materials included XRD, scanning and transmission electron microscopy coupled with energy dispersive spectroscopy (SEM/EDS and TEM/EDS), determination of the specific surface area by the Brunauer, Emmett, and Teller (BET) technique, and measurements of total conductivity (four-probe direct current); description of the experimental techniques and equipment is found elsewhere ([20–23] and references cited). Thermogravimetric analysis used to estimate oxygen stoichiometry from the weight changes was performed on a Setaram SetSys 16/18 instrument; the measurements regime included heating (3 °C/min) in flowing air up to 900 °C, flushing of the apparatus with argon for 1 h, and then reduction at 900 °C in flowing 10%H_2–90%N_2 mixture. The cation composition of selected samples was confirmed by the inductively coupled plasma spectroscopic analysis (Jobin Yvon, model JY 70 plus).

For the electrochemical measurements, dense ceramic disks were polished with SiC abrasive paper and diamond pastes, followed by ultrasound washing with acetone and distilled water. To provide ohmic contact, Pt paste was deposited on the back side of the disks and annealed at 1,000 °C, then a copper current collector was connected to the Pt layer using a silver paste, and the electrode back side was isolated by an Araldite epoxy resin. The measurements were performed using an Autolab PGSTAT20 potentiostat and a conventional three-electrode two-compartment Pyrex glass cell. A Pt foil and an Hg/HgO/KOH (1 M) electrode were used as the counter and reference electrodes, respectively. The current-interrupt internal resistance (IR) compensation technique was employed to measure ohmic drop between the Luggin capillary and working electrode; the IR-free polarization curves were obtained subtracting ohmic drop from the measured potential. For the electrochemical impedance spectroscopy, a Gamry PCI4/750 potentiostat (frequency range 0.01 Hz to 50 kHz, 10 points per decade, 10 mV signal amplitude) and a Pt foil counter electrode with the surface area 25–30 times larger than that of the working electrode were used.

Results and discussion

Materials characterization

XRD analysis confirmed formation of single perovskite-type phases in $La_{1-x}Sr_xCoO_{3-\delta}$ (x=0.3–0.7), $(La_{0.3}Sr_{0.7})_{0.97}CoO_{3-\delta}$, and $La_{0.3}Sr_{0.7}Co_{0.8}Al_{0.2}O_{3-\delta}$ powders and ceramics. For $La_{0.55}Sr_{0.40}CoO_{3-\delta}$ and $La_{0.65}Sr_{0.30}CoO_{3-\delta}$, minor impurity reflections corresponding to cobalt oxide (1–2%) were observed. The ABO_3 perovskite structure of all cobaltite materials containing more than 50% Sr in the A sublattice was identified as cubic; for cobaltites with lower Sr content, the lattice is rhombohedrally distorted. The ceramics of $La_2Ni_{1-x}Me_xO_{4+\delta}$ (Me=Co, Cu) were all found to be single phase, with tetragonal K_2NiF_4-type structure. These results and the values of unit-cell parameters, oxygen nonstoichiometry, and Co^{4+} concentration in the cobaltite solid solutions (Table 1 and Fig. 1) are in a good agreement with literature (e.g., [17, 18] and references therein). SEM inspection showed that all dense ceramic materials have a similar microstructure; the average grain size was 2–10 μm. Except for $La_{0.55}Sr_{0.40}CoO_{3-\delta}$ and $La_{0.65}Sr_{0.30}CoO_{3-\delta}$ where cobalt oxide segregation occurs in the form of small grains, EDS analysis confirmed homogeneous cation distribution within the limits of experimental uncertainty.

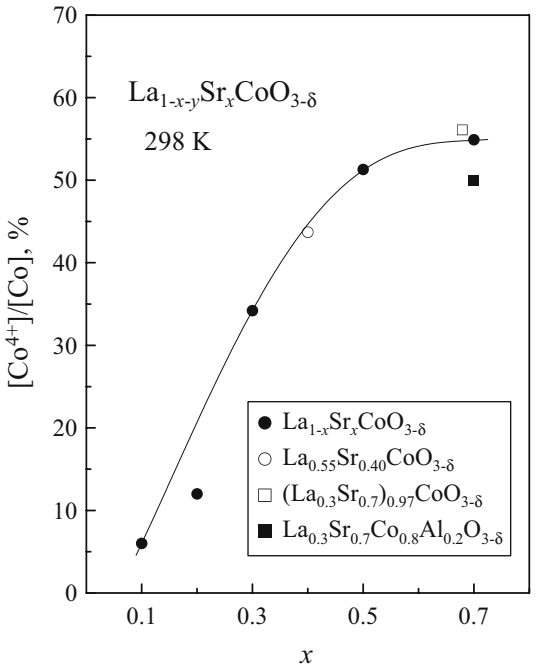

Fig. 1 Dependence of the $[Co^{4+}]/[Co]$ ratio on strontium content in lanthanum–strontium cobaltite materials at room temperature, calculated from the TGA data

The microstructures obtained during fabrication of microporous layers are illustrated by Figs. 2, 3, and 4. As expected [20], the materials synthesized from cellulose precursors retain microstructure of initial fibers (Fig. 2a, e, and i). The use of A- and B-type precursors results in similar, uniform microstructures of the porous layers and in a similar shrinkage (Fig. 2b–d and f–h, respectively), although the latter provides a moderately larger surface area. The specific surface-area values for the porous layers, made of the A- and B-type precursors, were 0.28 and 0.43 m^2/g, correspondingly. The use of the cotton bandage precursor (type C) leads to weakly consolidated cobaltite fibers (Fig. 2i) and to a significant shrinkage of the porous layer during sintering (cf. Fig. 2c, g, and k); this is associated with cracking (Fig. 2j) and lower porosity of cobaltite grains (Fig. 2l).

Figure 5 presents the bright- and dark-field TEM images of as-synthesized materials, all after annealing at 900 °C for 2 h. For the A- and B-type precursors, the particles consist of an amorphous matrix with embedded nuclei of perovskite phase, approximately 10–40 nm. Their crystallization occurs hence during sintering of the porous layers. The powders prepared using C-type cellulose precursor and GNP are both characterized with almost completely crystallized grains; one example of the electron diffraction pattern is shown in the inset of Fig. 5c.

Inspection of the multilayered anodes, comprising a layer of grained G-$(La_{0.7}Sr_{0.3})_{0.97}CoO_{3-\delta}$ deposited onto another (A-type) porous layer, showed a good cohesion between the particles (Fig. 3). In contrast to the materials prepared using cellulose precursors, where the grains have a specific fiber-like shape (Fig. 2d and h), GNP results in roundish particles with an essentially uniform grain size (Fig. 4). At the same time, the specific surface area of the porous layer fabricated using GNP, 0.34 m^2/g, remains similar to that of other layers.

Cyclic voltammetry

As the electrocatalytic activity to OER can be evaluated by measuring steady-state anodic voltammograms and normalizing these data to real area, an attempt to assess the roughness

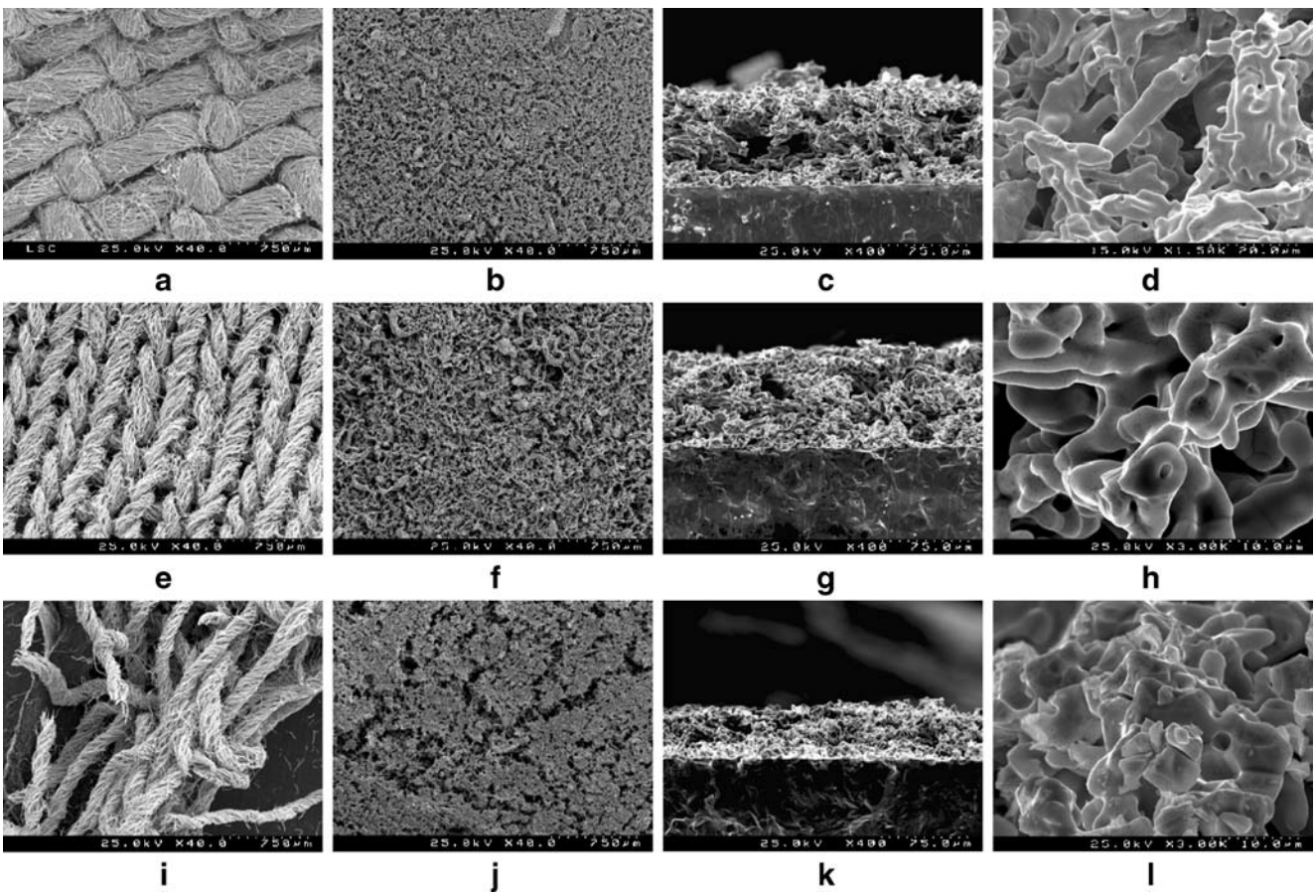

Fig. 2 SEM micrographs of $(La_{0.3}Sr_{0.7})_{0.97}CoO_{3-\delta}$ porous layers prepared using different cellulose precursors: **a**, **e**, **i** as-synthesized materials after annealing at 900 °C for 2 h, **b**, **f**, **j** top view of the porous layers after sintering at 1,200 °C, and **c**, **d**, **g**, **h**, **k**, **l** cross-sections with two different magnifications. The images **a**–**d**, **e**–**h**, and **i**–**l** correspond to the A-, B-, and C-type precursors, respectively

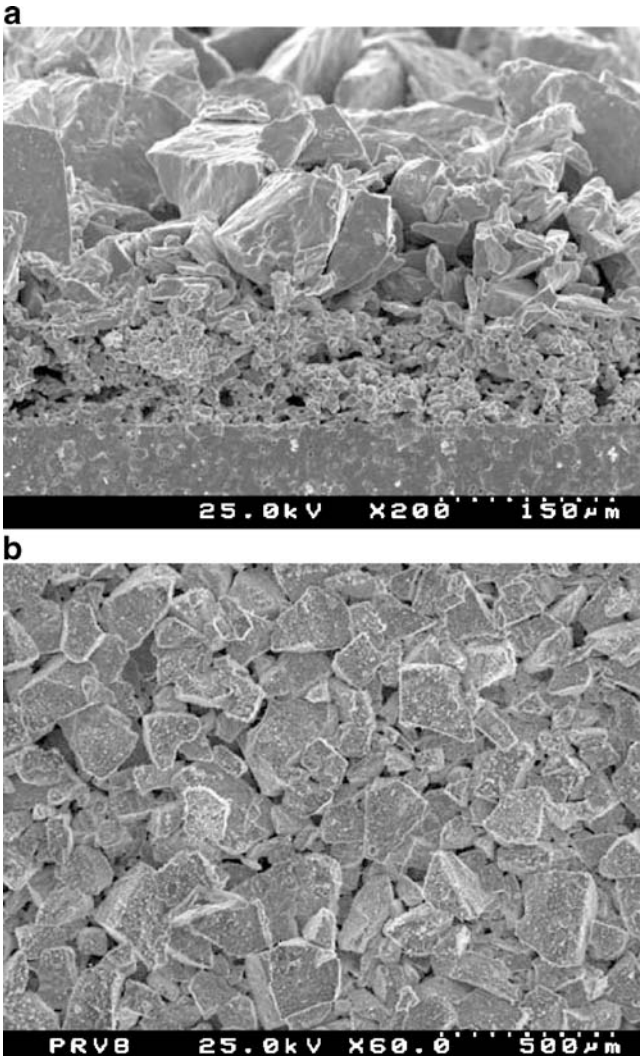

Fig. 3 SEM micrographs of three-layer electrode, where the top layer made of coarse-grained particles (G-$(La_{0.3}Sr_{0.7})_{0.97}CoO_{3-\delta}$) is deposited on the microporous layer of $(La_{0.3}Sr_{0.7})_{0.97}CoO_{3-\delta}$ synthesized from the A-type cellulose precursor

factor (σ) of polished ceramic electrodes was made to calculate the true current density. In theory, such estimations could be made from the values of capacitive current, measured by cycling the potential in a narrow range within a double-layer region near the rest potential, i.e., in the region free of pseudo-capacitive and faradaic currents [5, 13–15, 24]. However, for the title materials, the capacitance values corresponding to the charging current (C_{cap}, Table 2) are composition-dependent and differ substantially from 60 μF cm^{-2}, a commonly used estimate of the double-layer capacitance of an ideal oxide surface, C_{dl} [25]. This suggests that the simple ratio $\sigma=C_{cap}/C_{dl}$ cannot be assumed in the present case. Most likely, such behavior is due to faradaic contributions to the current recorded near the open-circuit potential (E_{ocp}), particularly associated with the electrochemical oxygen intercalation processes. For both perovskite-type cobaltites and K_2NiF_4-type nickelates in alkaline media, oxygen can be electrochemically intercalated into the lattice [7, 26–28]; this process was found reversible even at room temperature [28]. Indeed, the apparent C_{cap} values correlate with the oxygen deficiency of single-phase cobaltite materials (Tables 1 and 2), indicating an increase in faradaic currents when the oxygen-vacancy concentration increases. For dense electrodes, therefore, the current vs potential curves were normalized to the geometrical area.

For the electrodes with porous cobaltite layers, the cyclic voltammograms (CVAs) measured in a narrow potential range near E_{ocp} display significant asymmetry of the anodic and cathodic branches, again indicating a superimposition of the faradaic and charging currents. In this case, the true current density was hence estimated using the BET data.

The results presented below show that after operation under OER conditions, the performance of lanthanum–strontium cobaltite anodes becomes governed by the mixed

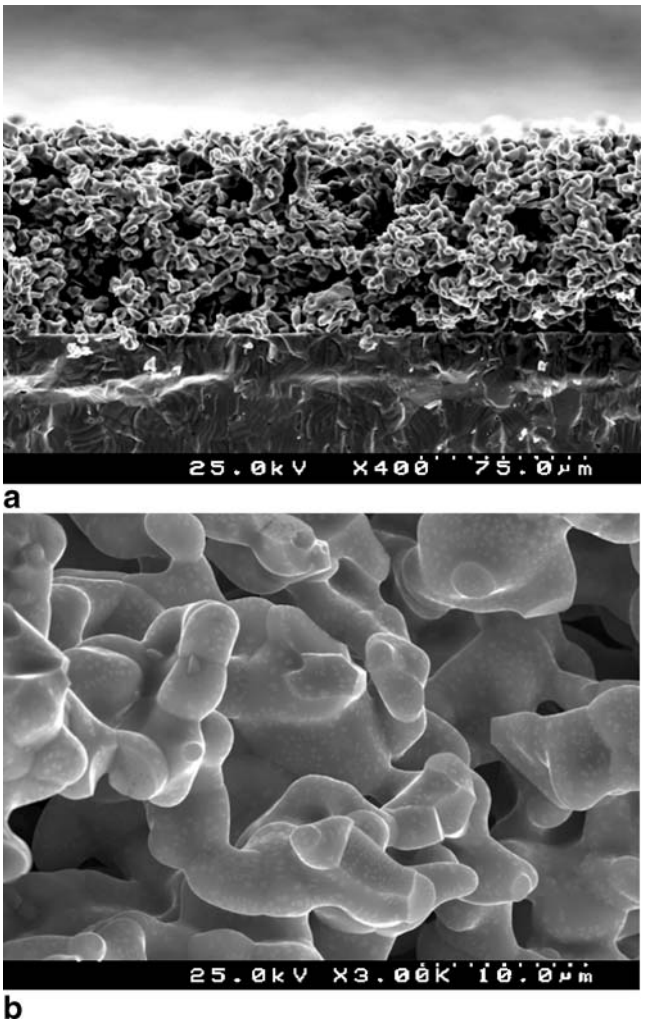

Fig. 4 SEM micrographs of the GNP-synthesized $(La_{0.3}Sr_{0.7})_{0.97}CoO_{3-\delta}$ porous layer deposited onto dense $La_{0.5}Sr_{0.5}CoO_{3-\delta}$ substrate

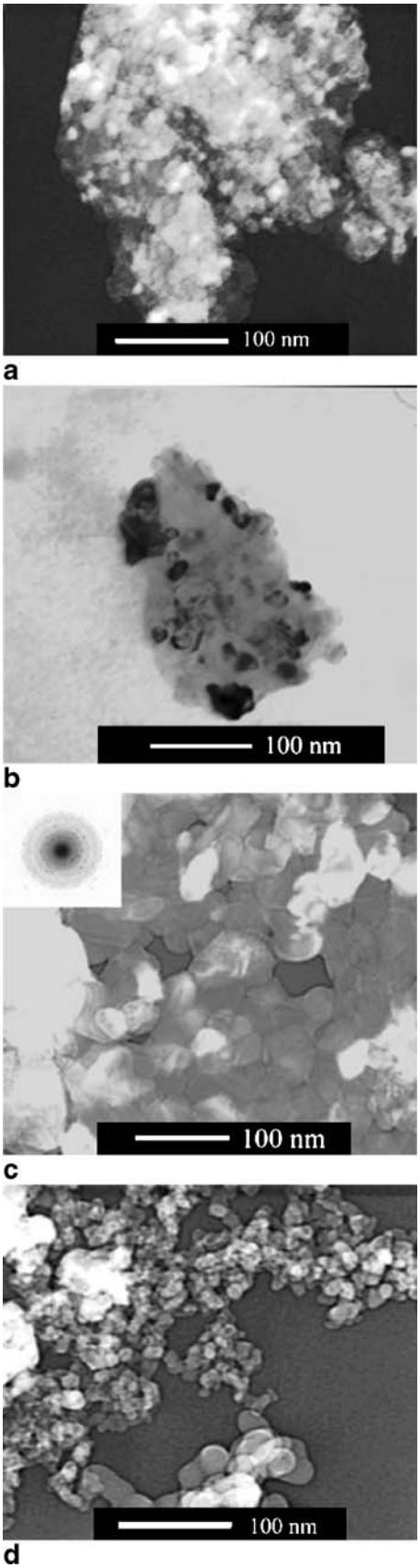

Fig. 5 TEM images of as-synthesized $(La_{0.3}Sr_{0.7})_{0.97}CoO_{3-\delta}$ powders prepared using different precursors: **a** A type, **b** B type, **c** C type, **d** GNP

hydroxide film formed on the surface. To access hydration-related effects, a series of lanthanum–cobalt and nickel hydroxide films were separately studied. Notice that nickel and cobalt oxides and hydroxides are well known to possess a high electrocatalytic activity for the OER [1–4]; when two or more metal oxides and/or hydroxides are present at the electrode surface, various synergetic effects are often observed [29–32]. In particular, the presence of strontium has a clearly positive influence on the activity of cobalt oxide-based electrodes [32]. In this work, the metal hydroxide layers were prepared on a Pt substrate by cathodic deposition from the corresponding metal nitrate solutions, where the process occurs because of increasing pH during the electrochemical reduction of nitrate ions [33]:

$$NO_3^- + H_2O + 2e^- \rightarrow 2OH^- + NO_2^- \quad (1)$$

This method is convenient to prepare mixed hydroxide films and has serious advantages with respect to alternative procedures [33, 34]. Figure 6a presents the CVAs of $Co(OH)_2$ and $Co(OH)_2$–$La(OH)_3$ composite films formed on Pt. Cobalt hydroxide exhibits a couple of redox peaks A_2/C_2 at 0.18 and 0.15 V, respectively, and a smaller anodic peak A_1 at 0.08 V. The A_2/C_2 peaks can be assigned to the reaction [35]:

$$Co_3O_4 + OH^- + H_2O \leftrightarrow 3CoOOH + e^- \quad (2)$$

The first anodic peak A_1 with weakly defined cathodic counterpeak might be associated with oxide formation:

$$3\,Co(OH)_2 + 2OH^- \leftrightarrow Co_3O_4 + 4\,H_2O + 2e^- \quad (3)$$

No extra signals are observed for codeposited $Co(OH)_2$ and $La(OH)_3$, while the magnitude and the ratio of peaks characteristic of the Co species are altered, probably because of morphological changes and intimate electronic interaction of the components. A similar couple of distinct peaks appear for the cobaltite electrodes after their long-term operation under OER conditions. Figure 6a presents one typical example, for dense $La_{0.5}Sr_{0.5}CoO_{3-\delta}$ after galvanostatic testing during 40 h. This indicates that cobalt oxide–hydroxide species are present at the ceramic electrode surface. No peaks are observed for as-prepared dense cobaltite electrodes in the potential range of 0.1–0.5 V. Analogously, applying microporous layers did not result in appearance of any signals when varying the potential from E_{ocp} to the onset of OER (Fig. 6b). On the contrary, when modifying the porous cobaltite layers with nickel–ferric hydroxide films, two coupled redox peaks become visible in the CVAs. These resemble the peaks characteristic of nickel hydroxide on metallic Ni [36, 37] and are thus

Table 2 Parameters of OER kinetics for the cobaltite- and nickelate-based electrodes in 1 M KOH solution at 25 °C

Electrode material	Tafel slope, (mV dec^{-1})	Current density (mA cm^{-2})		C_{cap} (μF cm^{-2})
		at E= 0.56 V	at E= 0.76 V	
$La_{0.3}Sr_{0.7}CoO_{3-\delta}$	59	2.45×10^{-2}	48.6	1.22×10^{2}
$(La_{0.3}Sr_{0.7})_{0.97}CoO_{3-\delta}$	58	4.26×10^{-2}	91.2	1.61×10^{3}
$La_{0.3}Sr_{0.7}Co_{0.8}Al_{0.2}O_{3-\delta}$	90/60[a]	2.69×10^{-1}	47.1	1.46×10^{3}
$La_{0.5}Sr_{0.5}CoO_{3-\delta}$	59	9.1×10^{-3}	18.3	21
$La_{0.55}Sr_{0.4}CoO_{3-\delta}$	57	1.15×10^{-2}	18.5	22
$La_{0.65}Sr_{0.3}CoO_{3-\delta}$	57	7.2×10^{-3}	17.4	46
$La_{0.7}Sr_{0.3}CoO_{3-\delta}$	61	8.5×10^{-3}	16.6	12
$La_2NiO_{4+\delta}$	77	–	–	–
$La_2Ni_{0.9}Co_{0.1}O_{4+\delta}$	80	–	–	–
$La_2Ni_{0.8}Cu_{0.2}O_{4+\delta}$	83	–	–	–

[a] The numbers correspond to the low (left) and high (right) overpotential ranges (see text).

ascribed to the quasi-reversible Ni(II)↔Ni(III) oxide transformation process.

Anodic polarization

Figure 7 shows typical anodic voltammograms for as-prepared dense cobaltite ceramics, measured sweeping the potential from E_{ocp} to more positive values. After initial sharp rise near E_{ocp} (0.07–0.15 V), the current increases moderately in the potential range up to approximately 0.5 V where the OER starts. In this range, the current magnitude rises substantially when strontium content increases above 50%. The maximum current density ($j>10^{-4}$ A cm^{-2}) is observed for $La_{0.3}Sr_{0.7}Co_{0.8}Al_{0.2}O_{3-\delta}$, the composition having a higher oxygen nonstoichiometry compared to other Co-containing perovskites (Table 1). Notice that prolonged testing under the conditions of extensive oxygen evolution ($E>0.65$ V) leads to a significant decrease in the current at 0.1–0.5 V. However, the current in this potential range increases again after keeping the electrode under open-circuit conditions.

Figure 8a and b compares the IR-free quasi-steady-state polarization curves for the anodic evolution of oxygen on different dense electrodes. Before the measurements, each electrode was preanodized during 30 min under a constant current density, 30 mA cm^{-2} for cobaltites and 10 mA cm^{-2} for nickelates, to stabilize the electrode surface. For most cobaltites (Fig. 8a), the OER up to 0.2 A cm^{-2} is characterized by a single Tafel line; the slope is close to 60 mV dec^{-1}, in agreement with data on similar compounds [5, 6, 8–11, 13, 14]. One exception relates to $La_{0.3}Sr_{0.7}Co_{0.8}Al_{0.2}O_{3-\delta}$ where the Tafel slope at overpotentials above 0.75 V is similar to other cobaltites but increases up to 90 mV dec^{-1} on decreasing polarization. In the low-overpotential range, the latter material appears to be the most active in comparison to other Co-containing perovskites. Such a behavior may be associated with oxygen intercalation competing with the OER. At higher overpotentials, the electrocatalytic activity decreases as $(La_{0.3}Sr_{0.7})_{0.97}CoO_{3-\delta} > La_{0.3}Sr_{0.7}CoO_{3-\delta} > La_{0.3}Sr_{0.7}Co_{0.8}Al_{0.2}O_{3-\delta} > La_{0.55}Sr_{0.40}CoO_{3-\delta} \approx La_{0.5}Sr_{0.5}CoO_{3-\delta} > La_{0.65}Sr_{0.30}CoO_{3-\delta} > La_{0.7}Sr_{0.3}CoO_{3-\delta}$. In the case of K_2NiF_4-type nickelate materials (Fig. 8b), the OER starts at $E>0.8$ V, and a straight Tafel line is observed up to high current densities, while the overpotentials are substantially higher than those of cobaltites. The Tafel slopes for the nickelate-based anodes are also higher, about 80 mV dec^{-1}. The apparent activation enthalpies for anode polarization, $(\Delta H_{el})_E$, were found essentially overpotential independent. One example is presented in Fig. 9, which shows the Arrhenius plots for dense $La_{0.5}Sr_{0.5}CoO_{3-\delta}$ electrode at two fixed potentials selected in the Tafel region. In the case of $La_{0.5}Sr_{0.5}CoO_{3-\delta}$, ΔH_{el} is about 72 kJ mol^{-1}, close to literature data [6] on $La_{0.8}Sr_{0.2}CoO_{3-\delta}$ (76.4 kJ mol^{-1}) and $La_{0.6}Sr_{0.4}CoO_{3-\delta}$ (74.3 kJ mol^{-1}).

Figure 8c and d presents the IR-corrected Tafel plots for the multilayer electrodes prepared depositing nanostructured cobaltite powders onto dense ceramics; the current density is calculated for the geometric electrode area. Applying porous layers leads to significantly lower OER overpotentials, as expected. For all electrodes, the Tafel slope is close to 60 mV dec^{-1} (Table 3), in agreement with the references [5, 6, 8, 9, 11, 13–16]. The microstructural differences between porous layers (Figs. 2 and 4) have a modest influence on the polarization; the corresponding overpotential changes are comparable to the reproducibility error for similar samples prepared under identical conditions (Fig. 8c). Analogously, increasing thickness of the microporous layer has an almost negligible effect; the deposition of passivated G-$(La_{0.7}Sr_{0.3})_{0.97}CoO_{3-\delta}$ layer increases polarization at high current densities (Fig. 8d). At the same time, the microporous layers applied onto $La_{0.3}Sr_{0.7}CoO_{3-\delta}$ ceramics provide lower overpotentials compared to $La_{0.5}Sr_{0.5}CoO_{3-\delta}$, because of higher electrochemical activity of the former composition. These results

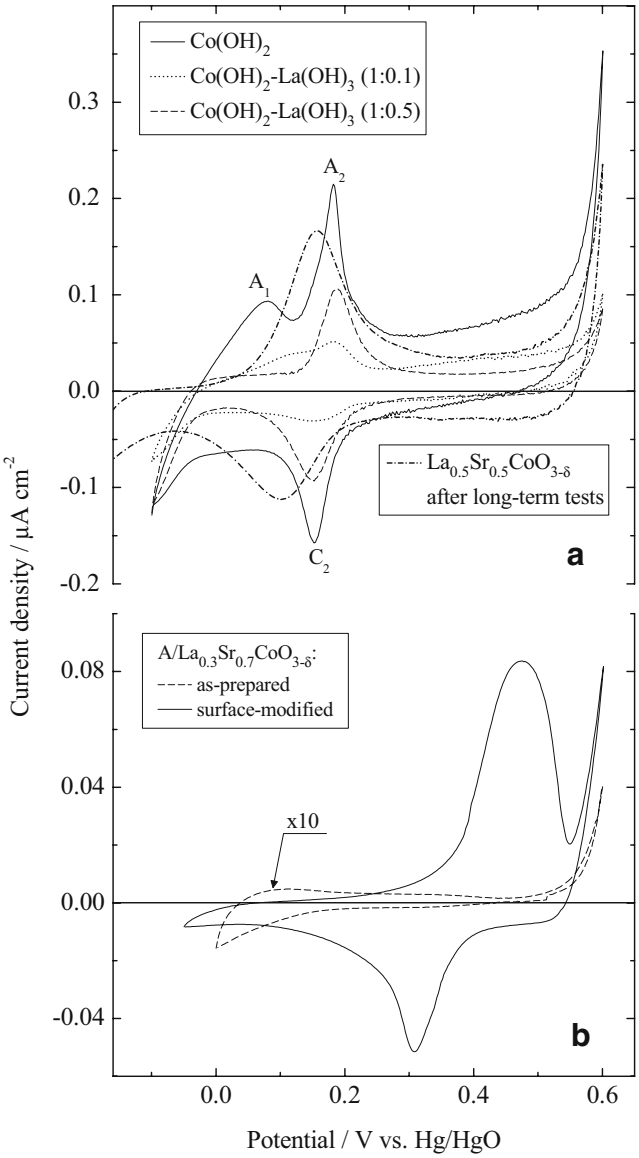

Fig. 6 Cyclic voltammograms in 1 M KOH solution at 25 °C: **a** comparison of the $Co(OH)_2$ and $Co(OH)_2$–$La(OH)_3$ films electrodeposited onto Pt and dense $La_{0.5}Sr_{0.5}CoO_{3-\delta}$ electrode after prolonged galvanostatic polarization (j=50 mA cm^{-2}, 40 h), at the potential scan rate of 5 mV s^{-1}; **b** A-type porous layer on dense $La_{0.3}Sr_{0.7}CoO_{3-\delta}$ substrate, after preparation and after surface modification with $Ni(OH)_2$–$Fe(OH)_3$ film, which was cathodically deposited from 1 M $Ni(NO_3)_2$+10^{-2} M $Fe(NO_3)_3$ solution at j=−1 mA cm^{-2} for 55 min. The $Co(OH)_2$ and composite $Co(OH)_2$–$La(OH)_3$ (1:0.1) and $Co(OH)_2$–$La(OH)_3$ (1:0.5) films in **a** were cathodically deposited onto Pt foil (j=−1 mA cm^{-2}; 30 min) from 1 M $Co(NO_3)_2$, 1 M $Co(NO_3)_2$+0.1 M $La(NO_3)_2$, and 1 M $Co(NO_3)_2$+0.5 M $La(NO_3)_3$ solutions, respectively

show that the electrochemical reaction is essentially localized in a narrow zone near the interface between porous and dense components; a significant part of the microporous layer has a minor contribution to the OER rate. The latter phenomenon may originate from trapping gas bubble formation and electronic transport limitations in the porous layer; in addition, mass-transport limitations

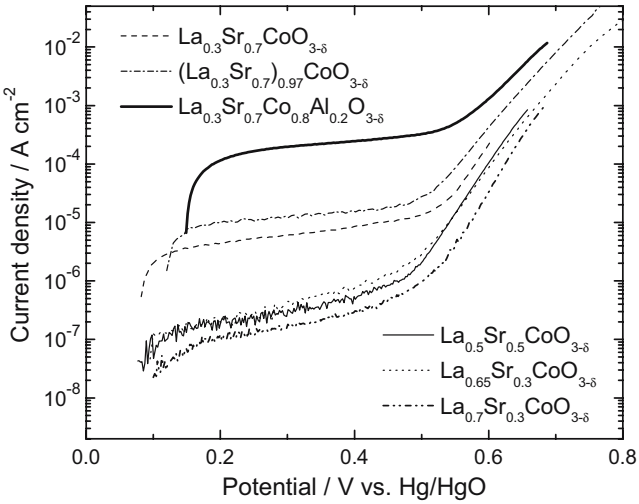

Fig. 7 Anodic polarization curves of as-prepared dense $La_{1-x-y}Sr_xCo_{1-z}Al_zO_{3-\delta}$ electrodes in 1 M KOH solution at 25 °C (the potential sweep rate is 1 mV s^{-1})

may appear when the current increases. Nonetheless, the average current densities normalized to the specific surface area measured by the BET technique are substantially higher than those reported for $(La, Sr)CoO_{3-\delta}$ films prepared using sol–gel routes [15, 16]. As an example, for highly dispersed $La_{0.5}Sr_{0.5}CoO_{3-\delta}$ films with a roughness factor of 2,580, the true current density at 0.4 V was 38.4 μA cm^{-2} [16]. The corresponding values, estimated from the apparent current densities (Table 3) and BET surface area for the cellulose precursor- and GNP-synthesized $(La_{0.3}Sr_{0.7})_{0.97}CoO_{3-\delta}$ layers, vary in the range 140–630 μA cm^{-2}.

Figure 8e compares the IR-free anodic polarization curves for $La_{0.5}Sr_{0.5}CoO_{3-\delta}$, cobalt hydroxide, and cobalt–lanthanum-mixed hydroxide films. $Co(OH)_2$ exhibits a linear Tafel dependence; the slope is approximately 50 mV dec^{-1}. The introduction of lanthanum hydroxide increases both the OER overpotential and, for 50% La cations, rises the slope. The mixed $La(OH)_3$–$Co(OH)_2$ films where the La/Co cation ratio is 0.5 shows a Tafel slope of approx.

Fig. 8 IR-free Tafel plots for oxygen evolution in 1 M KOH solution at 25 °C: **a** dense $La_{1-x-y}Sr_xCo_{1-z}Al_zO_{3-\delta}$ electrodes; **b** dense La_2NiO_4-based electrodes; **c** cellulose precursor- and GNP-synthesized porous layers deposited onto dense $La_{0.5}Sr_{0.5}CoO_{3-\delta}$; **d** cellulose precursor- and GNP-synthesized porous layers deposited onto dense $La_{0.3}Sr_{0.7}CoO_{3-\delta}$; **e** comparison of $Ni(OH)_2$, $Co(OH)_2$, and $Co(OH)_2$–$La(OH)_3$ films deposited onto Pt and dense $La_{0.5}Sr_{0.5}CoO_{3-\delta}$ electrode; **f** A-type porous layer on dense $La_{0.3}Sr_{0.7}CoO_3$ substrate after preparation and after deposition of $Ni(OH)_2$–$Fe(OH)_3$ film. All curves were recorded after pretreatment under anodic galvanostatic polarization (30 mA cm^{-2} for cobaltites and 10 mA cm^{-2} for nickelates) during 30 min. For the legends in **c** and **d**, the *numbers in parentheses* show loading density of the porous layers (in mg/cm^2) ▶

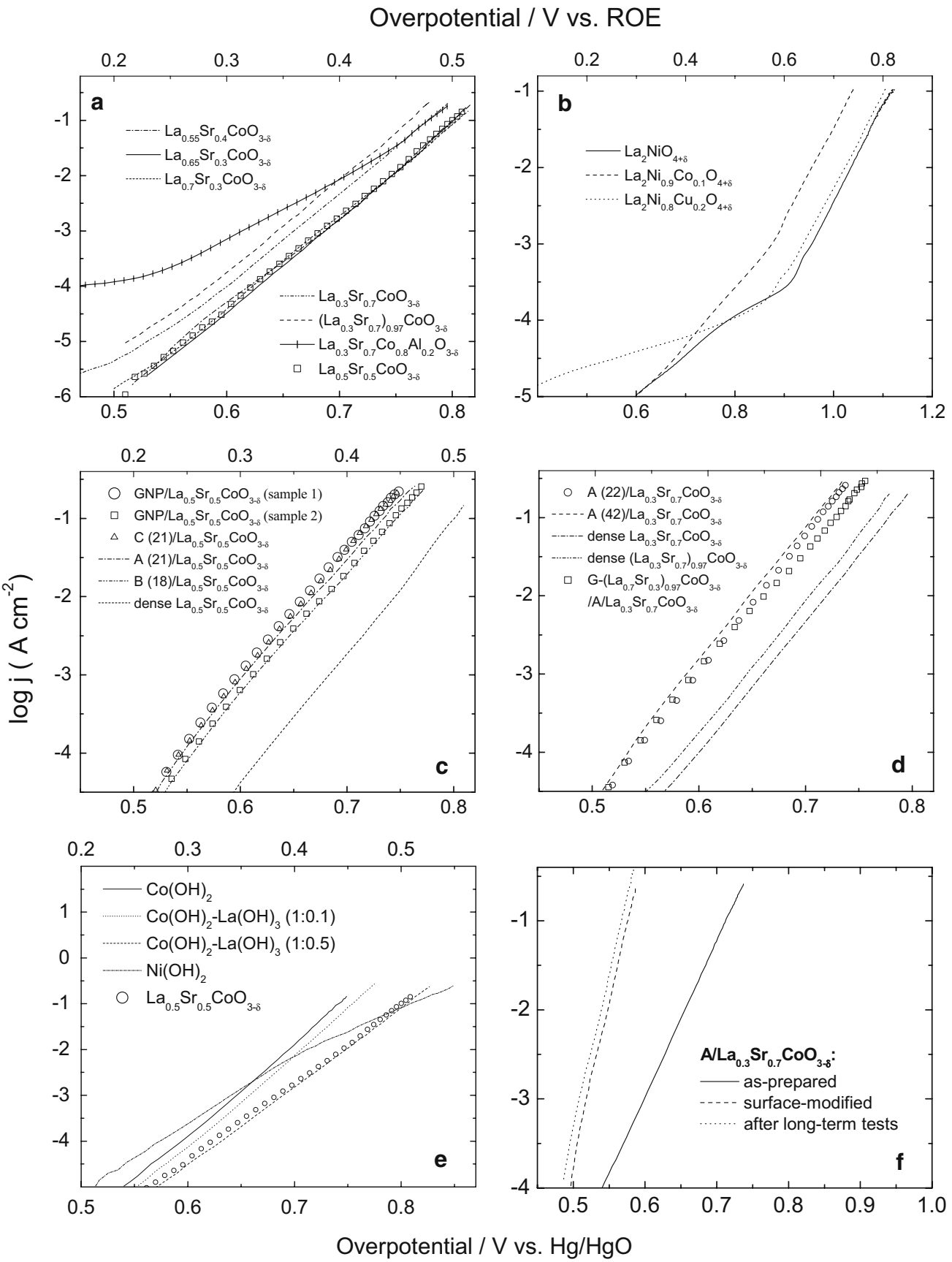
Overpotential / V vs. ROE
log j (A cm-2)
Overpotential / V vs. Hg/HgO
a
La0.55Sr0.4CoO3-δ
La0.65Sr0.3CoO3-δ
La0.7Sr0.3CoO3-δ
La0.3Sr0.7CoO3-δ
(La0.3Sr0.7)0.97CoO3-δ
La0.3Sr0.7Co0.8Al0.2O3-δ
La0.5Sr0.5CoO3-δ
b
La2NiO4+δ
La2Ni0.9Co0.1O4+δ
La2Ni0.8Cu0.2O4+δ
c
GNP/La0.5Sr0.5CoO3-δ (sample 1)
GNP/La0.5Sr0.5CoO3-δ (sample 2)
C (21)/La0.5Sr0.5CoO3-δ
A (21)/La0.5Sr0.5CoO3-δ
B (18)/La0.5Sr0.5CoO3-δ
dense La0.5Sr0.5CoO3-δ
d
A (22)/La0.3Sr0.7CoO3-δ
A (42)/La0.3Sr0.7CoO3-δ
dense La0.3Sr0.7CoO3-δ
dense (La0.3Sr0.7)0.97CoO3-δ
G-(La0.7Sr0.3)0.97CoO3-δ /A/La0.3Sr0.7CoO3-δ
e
Co(OH)2
Co(OH)2-La(OH)3 (1:0.1)
Co(OH)2-La(OH)3 (1:0.5)
Ni(OH)2
La0.5Sr0.5CoO3-δ
f
A/La0.3Sr0.7CoO3-δ:
as-prepared
surface-modified
after long-term tests

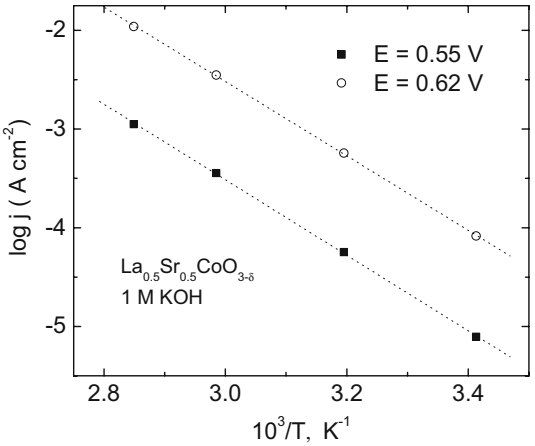

Fig. 9 Arrhenius plots for the oxygen evolution reaction on dense $La_{0.5}Sr_{0.5}CoO_{3-\delta}$ electrode in 1 M KOH solution

60 mV dec^{-1} as for $La_{0.5}Sr_{0.5}CoO_{3-\delta}$ (Table 2). These results and very similar peaks in the voltammograms (Fig. 6a) provide strong evidence that the operation of lanthanum–strontium cobaltite electrodes in alkaline media leads to the formation of mixed hydroxide films, determining the anode performance. On the other hand, additional studies are necessary to evaluate the effects of strontium hydroxide formation, although the literature data [32] suggest that the latter may promote OER on cobalt oxide–hydroxide film. In the case of La_2NiO_4-based electrodes where the concentration of lanthanum and the capacity for oxygen intercalation [7, 17, 25] are both higher, no quantitative comparison with nickel hydroxide-based films can be made. The reasons include progressive surface changes of $La_2Ni(Me)O_{4+\delta}$ ceramics, discussed below, and a greater role of the intercalation processes compared to perovskite-type cobaltites. Note that for the nickel hydroxide film, the Tafel slope is 66 mV dec^{-1} at overpotentials lower than 0.7 V and increases on increasing polarization because of changing Ni oxidation state (Fig. 8e).

The deposition of the $Ni(OH)_2$–$Fe(OH)_3$ film onto the surface of microporous cobaltite layers leads to a substantially higher electrochemical activity (Fig. 8f). For example, at j=100 mA cm^{-2}, the decrease in the overpotential is about 0.13 V; the Tafel slope decreases from 57 down to 29 mV dec^{-1}. A similar change in the Tafel slope, observed on iron doping of nickel hydroxide films, was explained by changing OER mechanisms [30]. On increasing solution temperature up to 80 °C, the OER overpotential of surface-modified electrodes with porous $(La_{0.3}Sr_{0.7})_{0.97}CoO_{3-\delta}$ layers becomes as low as 0.21 V at apparent current density of 100 mA cm^{-2}; the activation enthalpy is 79.3 kJ mol^{-1} (Fig. 10).

Stability

The stability of ceramic electrodes was evaluated analyzing time degradation of the anode potentials under galvanostatic conditions, with subsequent SEM/EDS inspections. The typical E vs time dependencies at the initial stage, after starting the operation of as-prepared electrodes, are given in Fig. 11a–d. The maximum changes are observed during first 5–10 min, then the anode potentials tend to stabilize, although a moderate decrease can be detected during 2–7 h for dense cobaltite electrodes because of the formation of thin hydroxide films on their surface. Nevertheless, in this case, the SEM/EDS analysis revealed no substantial alterations of the surface morphology. On the contrary, the morphology of nickelate-based anodes suffers dramatic changes even after short-term tests. Relatively thick dark brown films are formed on the nickelate surface after 10–15 min anodic polarization at j=10 mA cm^{-2}; scraps of these layers exfoliate from the surface, thus increasing the roughness (Fig. 12). At the same time, EDS inspection showed that the Ni/La ratio in the surface layers is essentially unchanged with

Table 3 Parameters of OER kinetics for the cobaltite electrodes with porous layers in 1 M KOH solution at 25 °C

Porous layer and dense support	Sheet density of the porous layers (mg cm^{-2})	Tafel slope (mV dec^{-1})	Apparent current density[a] at 0.4 V overpotential (mA cm^{-2})
GNP/$La_{0.5}Sr_{0.5}CoO_3$	20	64	42.8
A/$La_{0.5}Sr_{0.5}CoO_{3-\delta}$	21	65	30.2
B/$La_{0.5}Sr_{0.5}CoO_{3-\delta}$	18	66	19.5
C/$La_{0.5}Sr_{0.5}CoO_{3-\delta}$	21	62	38.0
A/$La_{0.3}Sr_{0.7}CoO_{3-\delta}$	22	57	59.6
A/$La_{0.3}Sr_{0.7}CoO_{3-\delta}$	42	59	81.3
Grained G-$(La_{0.7}Sr_{0.3})_{0.97}CoO_{3-\delta}$/A/$La_{0.3}Sr_{0.7}CoO_{3-\delta}$	19/76	63	36.5

[a] The values are related to the geometric electrode area.

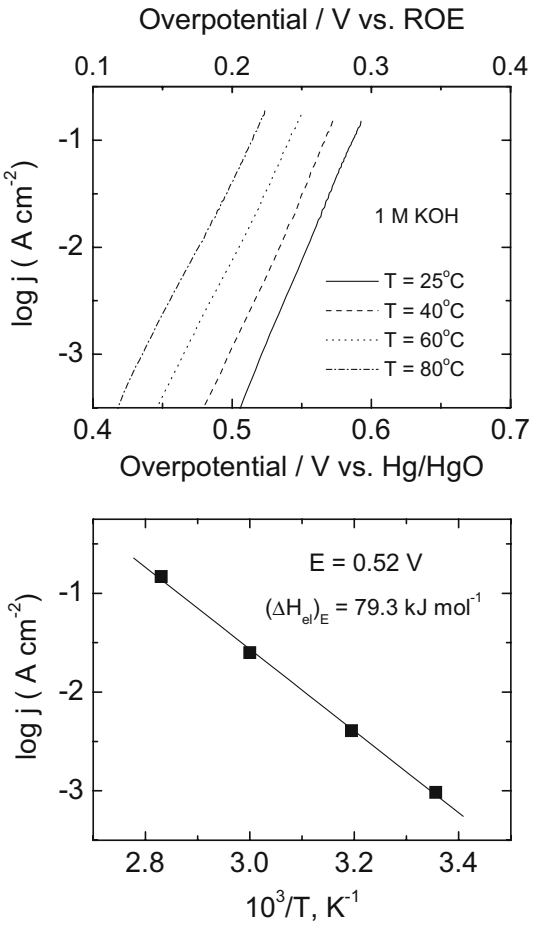

Fig. 10 Tafel plots for the OER on A-type porous layer deposited onto dense $La_{0.3}Sr_{0.7}CoO_{3-\delta}$ ceramics with subsequent surface modification with $Ni(OH)_2$–$Fe(OH)_3$ film, and the corresponding Arrhenius plot

respect to the bulk composition. Taking into account the data on oxygen intercalation into $La_2NiO_{4+\delta}$ [7, 26, 28], the latter phenomena were attributed to the surface oxidation of $La_2Ni_{1-x}Me_xO_{4+\delta}$ and phase decomposition, resulting in the formation of NiOOH and $La(OH)_3$. The large range of possible oxygen-nonstoichiometry variations [7, 17, 26] and the higher concentration of lanthanum in $La_2Ni_{1-x}Me_xO_{4+\delta}$ in comparison to perovskite-type cobaltites explain the differences in anodic behavior of these compounds.

Figure 11c shows selected results of the stability tests of $La_{0.5}Sr_{0.5}CoO_{3-\delta}$ electrodes coated with various porous layers, compared to the data on polished $La_{0.5}Sr_{0.5}CoO_{3-\delta}$ ceramics. In contrast to dense anodes, the presence of porous layers leads to a moderate reversible increase in the potential under galvanostatic polarization during the first 10–20 min. The reversibility of such behavior is illustrated by Fig. 13. During potential scan without preanodization, a decrease in the current is observed at high overpotentials, leading to deviations from the Tafel dependence; the second scan after preanodization in the OER region gives a linear Tafel plot with slightly lower currents, which can then be increased keeping the electrode under open-circuit conditions for 0.5–1 h (cf. curves 1–3 in Fig. 13). These effects may result from partial blocking of the electrochemically active area by O_2 bubbles and/or from local pH changes in the porous layer [38]. Whatever the mechanism, no degradation is observed under galvanostatic polarization in a concentrated (30% NaOH) alkaline solution, where the potential even decreases with time (Fig. 11e); SEM inspection revealed no essential microstructural alterations after testing in strongly concentrated alkaline media. An essentially stable performance was also found after the deposition of the $Ni(OH)_2$–$Fe(OH)_3$ film on the surface of microporous layer (Fig. 11f).

Electrochemical impedance spectroscopy

Selected Nyquist plots of the dense cobaltite and nickelate-based electrodes in the OER potential range are presented in Fig. 14a. These data can be described by an equivalent circuit shown in Fig. 14b; the fitting results are shown in Fig. 14a as solid lines. The effective capacitance C_{eff} and faradaic admittance $Y_{\text{ct}}=R_{\text{ct}}^{-1}$ (Fig. 15) were calculated from the charge-transfer resistance R_{ct} and constant phase element parameters A and α, defined by the relationship $C_{\text{eff}} = A \times \omega_{\max}^{\alpha-1}$ where $\omega_{\max}$ is the frequency corresponding to maximum $-Z_{\text{im}}$. When collecting the data shown in Fig. 15, one impedance spectrum was initially recorded for the as-prepared $La_{0.5}Sr_{0.5}CoO_{3-\delta}$ at low anodic potential (0.2 V), far from the OER range, then the potential was shifted up to 0.5 V (the region near OER), increased up to 0.8 V, and scanned from 0.8 down to 0.5 V and in the reverse direction, with a 20-min delay at each E value. The capacitance C_{eff} is relatively low for the as-prepared electrode at overpotentials below the OER region but increases substantially after anodic polarization at $E>$ 0.6 V, in particular because of hydroxide film formation. The reversible decrease in C_{eff} on increasing overpotential in the OER range may be associated with partial blocking by oxygen bubbles. The Tafel slope calculated from the log Y_{ct} vs E curve (Fig. 15) is about 60 mV dec^{-1}, in excellent agreement with the polarization curves. Similar trends are observed for other cobaltite electrodes.

Near the open-circuit potential (0.04–0.15 V, depending on the electrode material), the EIS measurements of cobaltite anodes reveal several new features (Fig. 16a). The Bode plots recorded at E_{ocp} demonstrate two distinct time constants. As the first high-frequency constant disappears on further increase in the overpotential above 0.2 V, it can be assigned to the quasi-reversible Co^{2+}/Co^{3+} redox process occurring at the cobalt oxide–hydroxide

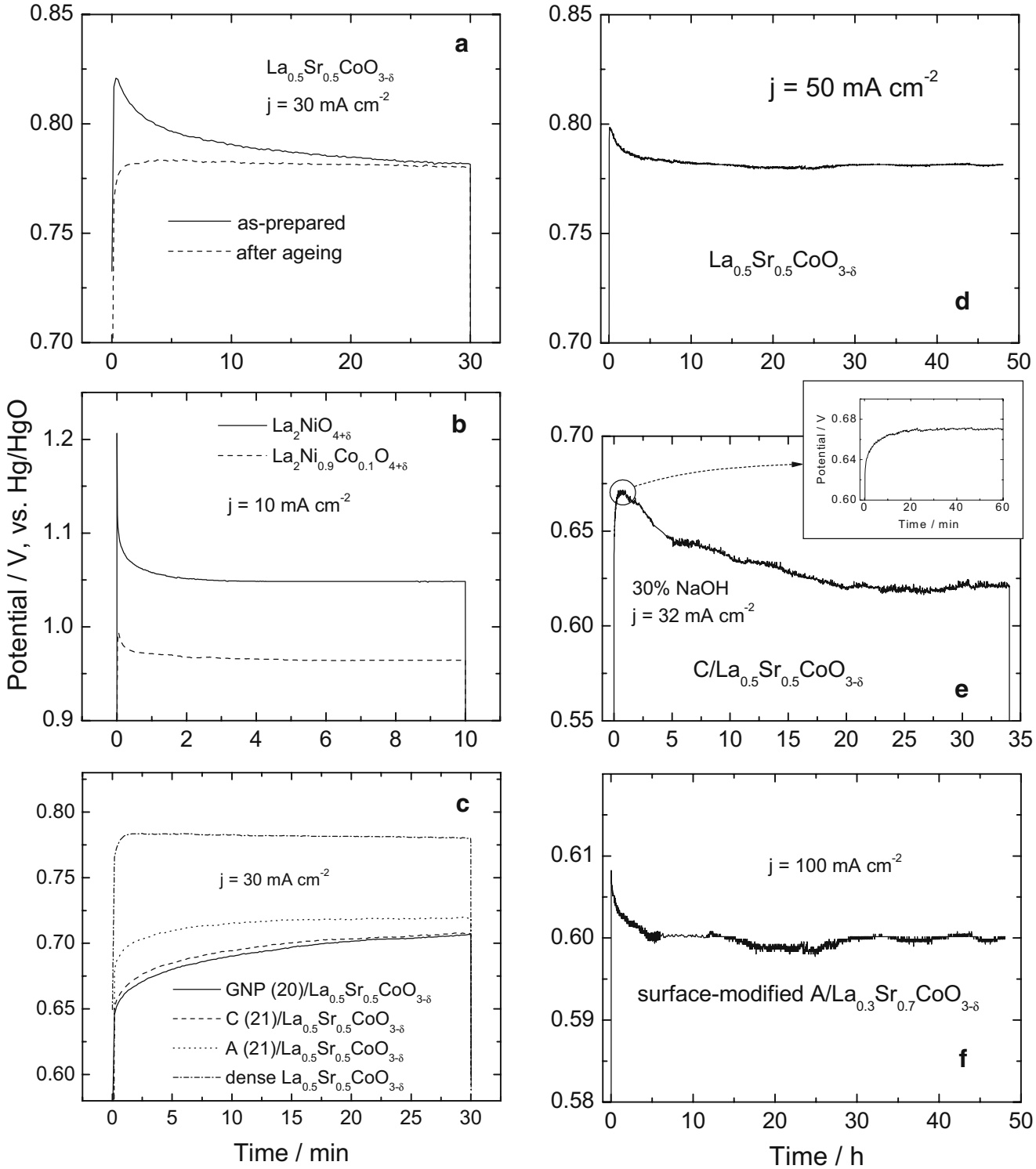

Fig. 11 Time dependencies of the electrode potential, measured at 25 °C in the galvanostatic regime without correction for IR drop: **a** dense $La_{0.5}Sr_{0.5}CoO_{3-\delta}$; **b** dense $La_2Ni_{1-x}Me_xO_{4+\delta}$; **c** cellulose- and GNP-synthesized porous layers deposited onto dense $La_{0.5}Sr_{0.5}CoO_{3-\delta}$; **d** dense $La_{0.5}Sr_{0.5}CoO_{3-\delta}$ under prolonged galvanostatic polarization; **e** C-type porous layer on dense $La_{0.5}Sr_{0.5}CoO_{3-\delta}$ substrate in strongly alkaline solution; **f** A-type porous layer on dense $La_{0.3}Sr_{0.7}CoO_{3-\delta}$ after surface modification with $Ni(OH)_2$–$Fe(OH)_3$. All data correspond to 1 M KOH solution, except for **e**. For the legend in **c**, the *numbers in parentheses* show the sheet density of porous layers (in mg/cm^2)

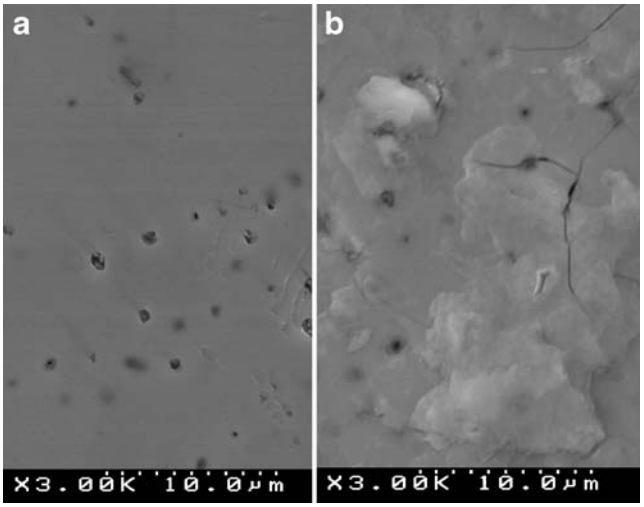

Fig. 12 SEM micrographs of $La_2NiO_{4+\delta}$ electrode: **a** after polishing, **b** after galvanostatic polarization (j=10 mA cm^{-2}, 10 min) in 1 M KOH solution

species in the outer layer of ceramic electrodes. This process corresponds to the couple of peaks observed in the CVAs after prolonged oxygen evolution (Fig. 6a). It is also noteworthy that the first time constant becomes more distinct for the electrodes aged under the OER conditions. Another time constant, at intermediate and low frequencies, is likely to result from oxygen electrointercalation into the ceramic material. The corresponding EIS spectra were successfully fitted using the equivalent circuit shown in Fig. 16b. The capacitance values for the first time constant were found low, 60–100 μF cm^{-2}, close to the possible double-layer capacitance of the electrode.

Final comments

The basic OER mechanisms, proposed for the conditions when the surface of cobaltite- and nickelate-based electrodes remains essentially unchanged in the course of electrolysis [5, 6, 8, 10], suppose that the rate-limiting step has a chemical nature associated with either desorption of OH surface groups or proton transfer from these groups to hydroxyl ions. The so-called peroxide mechanism [5, 8] comprises the following steps:

$$B_S + OH^- \leftrightarrow B_S - OH + e^- \quad (4a)$$

$$B_S - OH + OH^- \rightarrow B_S \ldots H_2O_2 + e^- \quad (4b)$$

$$(H_2O_2)_{phys} + OH^- \leftrightarrow \left(HO_2^-\right)_{phys} + H_2O \quad (4c)$$

$$(H_2O_2)_{phys} + \left(HO_2^-\right)_{phys} \leftrightarrow H_2O + OH^- + O_2 \quad (4d)$$

where B_S is the B-site cation (Co or Ni) located at the surface, and the step 4b is rate determining. According to this mechanism, the OER rate should increase with decreasing the B_S–OH bond strength. This may explain the variations of electrochemical activity in the $(La, Sr)CoO_{3-\delta}$ system (Fig. 8), as thermodynamic stability of such cobaltites and hence the metal–oxygen bond energy decrease on increasing concentration of Sr^{2+} ions and/or cation vacancies in the lanthanum sublattice (e.g., [17, 18] and references cited). In spite of the lower concentration of B-site cations in $La_2NiO_{4+\delta}$ compared to $LaNiO_3$-based perovskites, however, the assumptions [5, 8] cannot clarify the great difference in electrochemical performance of nickelate and cobaltite electrodes. Another possible reaction pathway:

$$B_S + OH^- \leftrightarrow B_S - OH + e^- \quad (5a)$$

$$B_S - OH + OH^- \rightarrow B_S - O^- + H_2O \quad (5b)$$

$$B_S - O^- \leftrightarrow B_S - O + e^- \quad (5c)$$

$$2B_S - O \leftrightarrow 2B_S + O_2 \quad (5d)$$

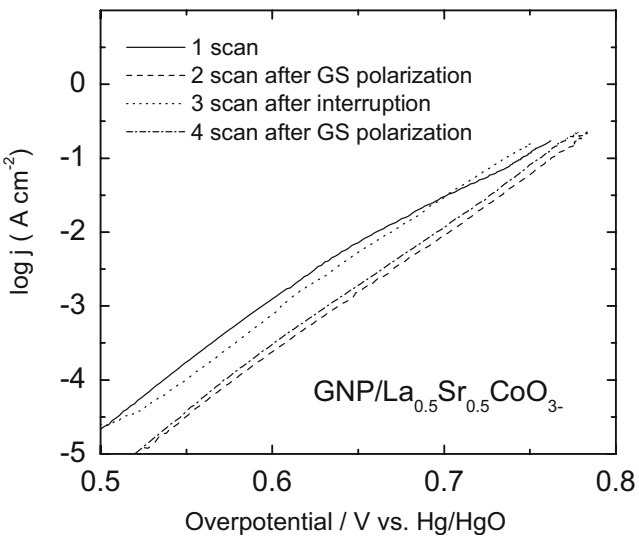

Fig. 13 IR-free Tafel plots for the oxygen evolution on GNP-synthesized porous layer deposited onto dense $La_{0.5}Sr_{0.5}CoO_{3-\delta}$. First scan was recorded on the as-prepared electrode, second scan—after the preanodization of the electrode in the OER region (j=30 mA cm^{-2}, 30 min), third scan—after keeping the electrode under open circuit conditions for 1 h, and fourth scan—again after preanodization in the OER region

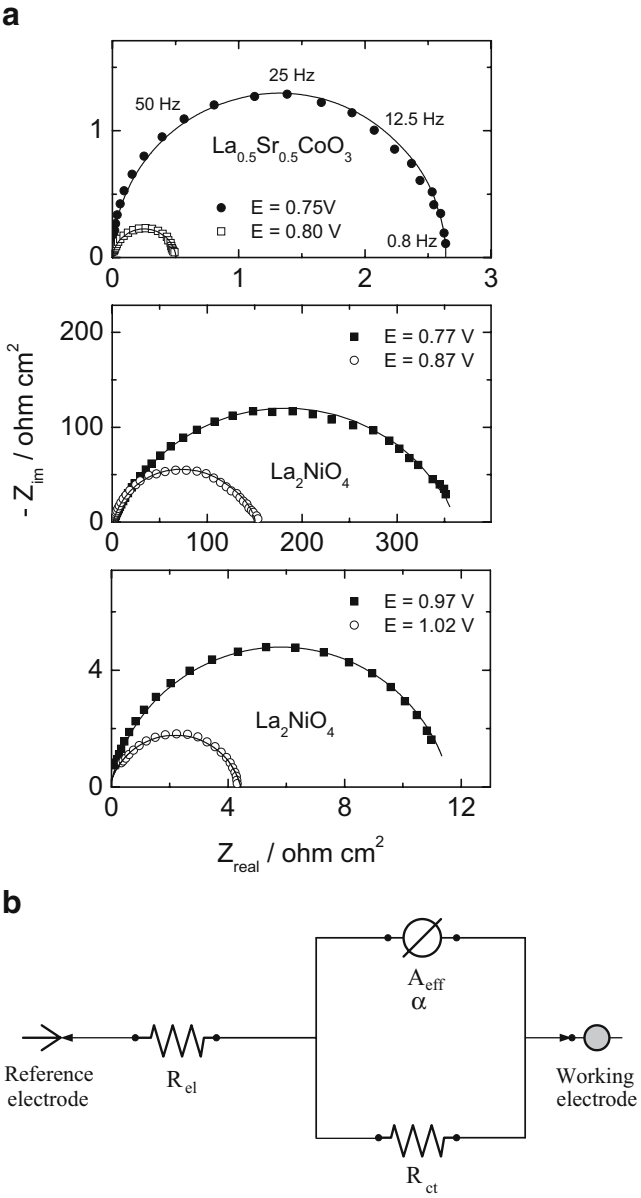

Fig. 14 Nyquist plots of cobaltite- and nickelate-based anodes in 1 M KOH solution at 25 °C (**a**) and the equivalent circuit used for analysis (**b**). The fitting results are shown by *solid lines*

with the rate-determining step 5b, is also well-known in literature [6, 10]. In this case, the electrocatalytic activity is expected to increase with positive charge of the B-site cations on the electrode surface, which facilitates proton detachment from the surface B_S–OH groups [6]. Indeed, comparison of the data on oxygen nonstoichiometry, B-site cation oxidation state, and electrochemical properties (Figs. 1, 7 and 8a, b, and Table 1) may confirm relevance of the latter factor in the high-overpotential range where OER is prevailing. In fact, the highest activity in the OER region is observed for $(La_{0.3}Sr_{0.7})_{0.97}CoO_{3-\delta}$ where the concentration of Co^{4+} is maximum; the lowest OER rate was found for $La_2NiO_{4+\delta}$ and $La_2Ni_{0.8}Cu_{0.2}O_{4+\delta}$ where the average oxidation state of B-site cations varies in the range from +2.24 to +2.30. Decreasing overpotentials to the values characterized by concurrence between the OER and oxygen intercalation leads to an increasing role of other factors, primarily oxygen storage capacity. Under these conditions, the maximum currents are found for $La_{0.3}Sr_{0.7}Co_{0.8}Al_{0.2}O_{3-\delta}$ where the oxygen deficiency is maximum and for $La_2Ni_{0.8}Cu_{0.2}O_{4+\delta}$ with minimum occupancy of the interstitial positions available for oxygen incorporation compared to other K_2NiF_4-type phases (Table 1). Note that after the OER tests at high anodic currents, a prolonged evolution of intercalated oxygen from the hyperoxidized surface layers of highly deficient cobaltites was observed, clearly visible as the gas bubble formation during dozens of minutes under the open-circuit conditions.

On the other hand, the relationships between cation composition and OER performance of the title materials may also be described by the formation of hydroxide layers during oxygen evolution, indicated by the cyclic voltammetry data (Fig. 6a). The similar electrochemical behavior of $(La, Sr)CoO_{3-\delta}$ ceramics and model hydroxide

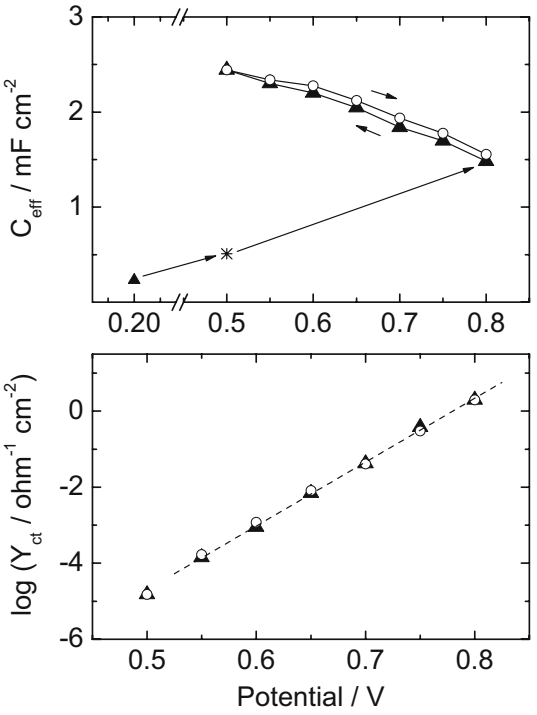

Fig. 15 Effective capacitance (C_{eff}) and faradaic admittance (Y_{ct}) as function of the potential of $La_{0.5}Sr_{0.5}CoO_{3-\delta}$ electrode vs Hg/HgO. The potential was changed in the following sequence: 0.2→0.5→0.8 (by 0.05-V steps)→0.5 (by 0.05-V steps)→0.8 V

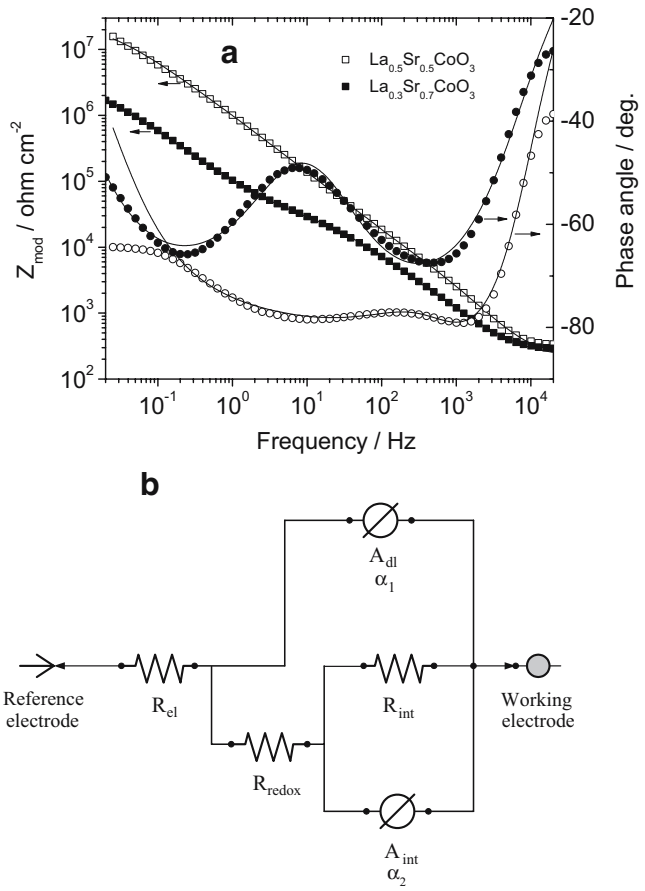

Fig. 16 Typical Bode plots of dense $La_{0.5}Sr_{0.5}CoO_{3-\delta}$ and $La_{0.3}Sr_{0.7}CoO_{3-\delta}$ electrodes under the open circuit potential in 1 M KOH solution (**a**) and the equivalent circuit used for fitting of the impedance spectra (**b**). The fitting results are shown by *solid lines*

layers electrodeposited onto Pt (Fig. 8e) supports this hypothesis. Because of high electrocatalytic activity of cobalt oxide–hydroxide, no decrease in the performance of $(La, Sr)CoO_{3-\delta}$ electrodes is observed when surface decomposition of the perovskite phase into hydroxides occurs. Furthermore, the resultant roughening of the electrode surface, accompanied with a significant increase in the effective capacitance (Fig. 15), seems responsible for decreasing overpotential with time (Fig. 11). If the activity of cobaltite electrodes in the OER region is indeed determined by the surface oxide–hydroxide layers, the overpotential variations in $(La, Sr)CoO_{3-\delta}$ system may be associated with changing the La/Co concentration ratio. The negative influence of $La(OH)_3$ addition is unambiguously revealed by the data on $Co(OH)_2$–$La(OH)_3$ composites (Fig. 8e). The same factor can be expected to impede OER kinetics on La_2NiO_4-based electrodes; the low electrochemical performance of nickelates correlates also with the behavior of $Ni(OH)_2$, which is less active than $Co(OH_2)$. Moreover, even the higher activity of $La_2Ni_{0.9}Co_{0.1}O_{4+\delta}$ in comparison with undoped $La_2NiO_{4+\delta}$ (Fig. 8b) seems to coincide with the cobalt-induced OER promotion on $Ni(OH)_2$ [39, 40].

Although the data obtained in this work are insufficient to unambiguously identify the OER mechanisms on perovskite-related ceramic anodes, the results show a key role of the electrode surface hydration and make it possible to select relevant trends necessary for future developments of highly active electrodes. In particular, for perovskite-type materials derived from $La_{1-x-y}Sr_xCoO_{3-\delta}$, the La/Co concentration ratio should be as low as possible, and the lattice should be La-deficient, within the solid solution formation limits. When the cation deficiency and/or dopant content are excessive, the secondary phase segregation leads to a change in the perovskite composition and thus decreases electrochemical performance. In the present work, this type of behavior is illustrated by the examples of $La_{0.55}Sr_{0.40}CoO_{3-\delta}$ and $La_{0.65}Sr_{0.30}CoO_{3-\delta}$ ceramics. The doping-induced oxygen deficiency of cobaltite electrodes promotes oxygen intercalation but has no essential effect on the behavior under high current densities in the OER region.

Finally, the maximum electrocatalytic activity is observed for $(La_{0.3}Sr_{0.7})_{0.97}CoO_{3-\delta}$, the composition close to the solid solution boundary. Further optimization of this material may include a moderate increase in the A-site deficiency, compensated by minor doping with higher-valence cations into the cobalt sublattice to maintain stability of the single perovskite-type phase. Attention should be drawn to the surface modification methods, including La depletion of the electrode surface layers to avoid lanthanum hydroxide formation under OER conditions, increasing specific surface area, and deposition of cobalt-hydroxide-based films. In particular, a significant decrease in the overpotentials was achieved applying microporous layers made of the cellulose precursor- and GNP-synthesized cobaltite, onto dense ceramics. However, the current densities and Tafel slopes observed for the layered anodes are weakly dependent of the thickness and morphology of the porous components, thus indicating that the reaction is localized in a narrow zone and making it necessary to optimize microstructural and geometrical parameters of the porous layers.

Acknowledgments This work was supported by the ULCOS program (CEC) and by the FCT, Portugal (projects POCI/CTM/59197/2004, REEQ/710/CTM/2005 and SFRH/BPD/28629/2006).

References

1. Trasatti S, Lodi G (1981) Oxygen and chlorine evolution at conductive metallic oxidanodes. In: Trasatti S (ed) Electrodes of conductive metallic oxides, part B. Elsevier, Amsterdam, pp 521–626
2. Matsumoto Y, Sato E (1986) Mater Chem Phys 14:397

3. Balej J (1985) Int J Hydrogen Energy 10:89
4. Trasatti S (1994) Transition metal oxides: versatile materials for electrocatalysis. In: Lipkowski J, Ross PN (eds) The electrochemistry of novel materials. VCH, New York, pp 207–295
5. Bockris JO'M, Otagawa T (1984) J Electrochem Soc 131:290
6. MatsumotoY,ManabeH,SatoE(1980)JElectrochemSoc127:811
7. Bhavaraju S, DiCarlo JF, Scarfe DP, Jacobson AJ, Buttrey DJ (1996) Solid State Ionics 86–88:825
8. Bockris JO'M, Otagawa T (1983) J Phys Chem 87:2960
9. Kobussen AGC, Van Buren FR, Van Den Belt TGM, Van Weers HJA (1979) J Electroanal Chem 96:123
10. Kobussen AGC, Mesters CMAM (1980) J Electroanal Chem 115:131
11. Willems H, Moers M, Broers GHJ, De Wit JHW (1985) J Electroanal Chem 194:305
12. Vondrak J, Dolezal L (1984) Electrochim Acta 29:477
13. TiwarySK,ChartierP,SinghRN(1995)JElectrochemSoc142:148
14. Jain AN, Tiwary SK, Singh RN, Chartier P (1995) J Chem Soc Faraday Trans 91:1871
15. Singh RN, Tiwary SK, Singh SP, Singh NK, Poillerat G, Chartier P (1996) J Chem Soc Faraday Trans 92:2593
16. Singh RN, Lal B (2002) Int J Hydrogen Energy 27:45
17. Kharton VV, Yaremchenko AA, Naumovich EN (1999) J Solid State Electrochem 3:303
18. Pena MA, Fierro JLG (2001) Chem Rev 101:1981
19. Murphy MW, Armstrong TR, Smith PA (1997) J Am Ceram Soc 80:165
20. Tsipis EV, Kharton VV, Bashmakov IA, Naumovich EN, Frade JR (2004) J Solid State Electrochem 8:674
21. Kharton VV, Tsipis EV, Yaremchenko AA, Frade JR (2004) Solid State Ionics 166:327
22. Kharton VV, Shaula AL, Vyshatko NP, Marques FMB (2003) Electrochim Acta 48:1817
23. Kharton VV, Tsipis EV, Marozau IP, Yaremchenko AA, Valente AA, Viskup AP, Frade JR, Naumovich EN, Rocha J (2005) J Solid State Electrochem 9:10
24. Trasatti S, Petrii OA (1991) Pure Appl Chem 63:711
25. Levine S, Smith AL (1971) Discuss Faraday Soc 52:290
26. Grenier J-C, Bassat J-M, Doumerc J-P, Etourneau J, Fang Z, Fournes L, Petit S, Pouchard M, Wattiaux A (1999) J Mater Chem 9:25
27. Magnone E, Cerisola G, Ferretti M, Barbucci A (1999) J Solid State Chem 144:8
28. Yazdi I, Bhavaraju S, DiCarlo JF, Scarfe DP, Jacobson AJ (1994) Chem Mater 6:2078
29. Cordoba SI, Carbonio RE, Lopez Teijelo M, Macagno VA (1986) Electrochim Acta 31:1321
30. Corrigan DA (1987) J Electrochem Soc 134:377
31. Wu G, Ni L, Zhou D-R, Mitsuo K, Xu B-Q (2004) J Solid State Chem 177:3682
32. Rotvin E, Brossard L (1995) J Appl Electrochem 25:462
33. Wohlfahrt-Mehrens M, Oesten R, Wilde P, Huggins RA (1996) Solid State Ionics 86–88:841
34. Streinz CC, Hartman AP, Motupally S, Weidner JW (1995) J Electrochem Soc 142:1084
35. Casella IG, Gatta M (2002) J Electroanal Chem 534:31
36. Jayashree RS, Kamath PV (2001) J Power Sources 93:273
37. Arulraj I, Trivedi DC (1989) Int J Hydrogen Energy 14:893
38. Evdokimov SV (1997) Russ J Electrochem 33:6
39. Unates ME, Folquer ME, Vilche JR, Arvia AJ (1992) J Electrochem Soc 139:2697
40. Zhang Y, Cao X, Yuan H, Zhang W, Zhou Z (1999) Int J Hydrogen Energy 24:529